

Planar Hall effect and quasi - 2D anisotropic superconductivity in topological candidate $1T$ -NbSeTe

C. Patra,¹ T. Agarwal,¹ Rajeshwari R. Chowdhury,¹ and R. P. Singh^{1,*}

¹*Department of Physics, Indian Institute of Science Education and Research Bhopal, Bhopal, 462066, India*

Superconducting topological materials have generated considerable interest in condensed matter research due to their unusual gap structures and topological properties. In this study, we have investigated the normal and superconducting characteristics of a potential topological semimetal $1T$ -NbSeTe through comprehensive transport and magnetization measurements on bulk single crystals. The results suggest the topological semimetallic nature of NbSeTe, evidenced by the observation of the planar Hall effect. Moreover, it displays quasi-2D anisotropic superconductivity, which breaks the Pauli limit. The coexistence of the topological semimetallic nature and superconductivity in NbSeTe makes it a potential contender for topological superconductivity.

I. INTRODUCTION

Superconductors and topological materials are distinct types of quantum materials, both displaying exceptional physical properties with potential applications. When combined, they can produce a distinct quantum phase called a topological superconductor (TSC) [1–3], representing a new paradigm for unconventional superconductivity. The TSC offers a novel platform to realize non-Abelian quasiparticle excitation, such as Majorana fermions, which can be used as a topological qubit for quantum computation [4, 5]. However, the realization of TSC in bulk topological materials is limited. Superconducting Dirac and Weyl semimetals have recently gained significant attention due to their non-trivial topology, as they provide a new platform to innovate TSCs [6–10]. Meanwhile, doped semimetallic topological transition metal dichalcogenides (TMDs) have emerged as a new platform to realize topological superconductivity [11].

Recent studies have revealed that the $1T$ phases of $M\text{Te}_2$ ($M = \text{Zr}, \text{Hf}, \text{Ni}, \text{Pt}, \text{Pd}, \text{Ir}$) [12–17], as well as the distorted $1T''$ phase of NbTe_2 [18], exhibit topological semimetallic behavior [19]. Further research suggests that superconductivity can be induced in these materials through strain, pressure, and doping [17], highlighting the potential for $1T$ phase materials as a platform for topological superconductivity. NbTe_2 has garnered significant interest due to its fascinating properties, such as magnetism, charge-density waves (CDW), superconductivity, and quantum spin Hall effect [19–21]. Though the $1T$ phase of NbTe_2 and NbSe_2 does not occur naturally in bulk crystals, the stable $1T''$ phase of NbTe_2 has been identified as a promising candidate for topological superconductivity, as topological semimetallic behavior and superconductivity ($T_c = 0.7$ K) coexist in this material [20, 22].

However, NbSeTe is unique in that it crystallizes in the $1T$ phase and exhibits enhanced superconductivity due to the suppression of CDW. The disorder is believed to play an important role in both suppressing and enhancing superconductivity in NbSeTe. Recent studies have shown that controlled disorder can enhance the superconducting transition temperature in monolayer NbSe_2 and $2H$ - $\text{TaSe}_{2-x}\text{S}_x$ by suppressing competing electronic orders, such as CDW [23–26]. Similar disorder-induced enhanced superconductivity has also been observed in bulk $2H$ - $\text{TaSe}_{2-x}\text{S}_x$. These studies suggest that disorder enhanced the electron-phonon coupling strength [27–31]. Thus, NbSeTe presents a unique opportunity to explore superconductivity in topological semimetals and the impact of the disorder on superconducting topological semimetals.

In this paper, we report the synthesis and properties of a single crystal of NbSeTe, which crystallizes in the structure $1T P\bar{3}m1$ (164). Our findings reveal that NbSeTe possesses a topological semimetallic nature, as demonstrated by the observation of the planar Hall effect. Furthermore, NbSeTe displays 2D-anisotropic superconductivity with a transition temperature of 3.16 K. The upper critical field surpasses the Pauli limiting field, and its proximity to the unconventional band in the Uemura plot suggests unconventional superconductivity.

II. EXPERIMENTAL METHODS

We prepared a single crystal of $1T$ -NbSeTe using the chemical vapor transport method. We mixed Nb (4N), Se (5N), and Te (5N) powders in a stoichiometric ratio and sealed them in a quartz tube with iodine (5 mg cm^{-3}) as the transport agent. The tube was then placed in a two-zone horizontal furnace with a temperature gradient of 950°C and 850°C . After 15 days; shiny single crystals were grown in the cold zone of the tube. The orientation of the crystal plane was determined by X-ray diffraction (XRD) using a PANalytical diffractometer

* rpsingh@iiserb.ac.in

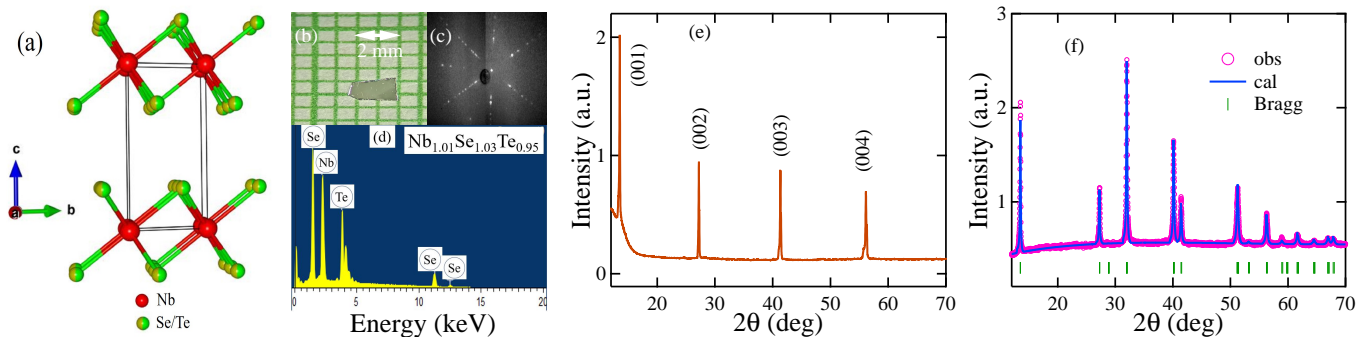


FIG. 1. (a) The unit cell structure of $1T$ -NbSeTe. (b) Shows the image of the single crystal. (c) The Laue diffraction pattern. (d) EDS scan that detects Nb, Se, and Te. (e) The X-ray diffraction pattern of the single crystal indicates that the crystal is oriented along the $[00l]$ plane. (f) Refinement of powder XRD data for determining lattice parameters.

equipped with $\text{CuK}\alpha$ radiation ($\lambda = 1.54056 \text{ \AA}$), and the Laue diffraction pattern was recorded using a Photonic-Science Laue camera. We used a scanning electron microscope (SEM) with an energy-dispersive X-ray (EDS) spectrometer to verify the sample compositions, which confirmed the presence of Nb, Se, and Te. Magnetization measurements were conducted using a Quantum Design magnetic measurement system (MPMS3), while resistivity and specific heat measurements were taken using a physical property measurement system (PPMS).

III. RESULTS AND DISCUSSION

a. Sample characterization

Fig. 1 shows the unit cell, single crystal image, Laue diffraction pattern, EDS measurements, and XRD patterns of $1T$ -NbSeTe. The unit cell, single-crystal image, and Laue diffraction pattern are depicted in (a), (b), and (c), respectively. EDS measurements in various areas of single crystals found the average elemental concentration to be $\text{Nb}_{1.01}\text{Se}_{1.03}\text{Te}_{0.95}$, as shown in (d). The XRD pattern of the single crystal, depicted in (e), confirms the crystal's orientation along the $(00l)$ direction. To determine the phase, we collected the XRD pattern of the crushed single-crystal powder, shown in (f). The powder XRD refinement confirms that the sample crystallizes in the trigonal $P\bar{3}m1$ (164) space group, with lattice parameters of $a = b = 3.56(5) \text{ \AA}$ and $c = 6.52(7) \text{ \AA}$ [29–31]. These lattice parameters are identical to those reported for $1T$ -NbSeTe [29].

b. Planar Hall effect

The planar Hall effect (PHE) is a phenomenon exhibited by topological semimetals (Dirac/Weyl) due to the chiral anomaly and non-trivial Berry curvature of these materials. PHE has been observed in several topological semimetals, including WTe_2 [32], Cd_3As_2 [8], ZrTe_5

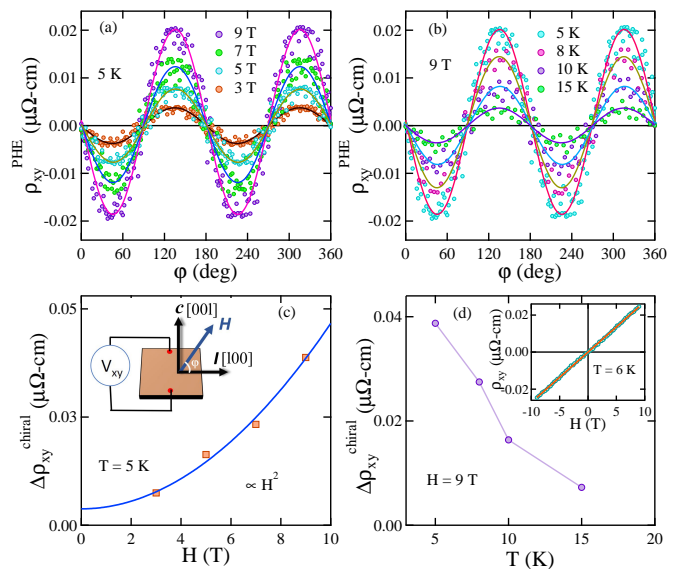


FIG. 2. (a) The planar Hall response for various applied magnetic fields at a temperature of 5 K. (b) Planar Hall effect at different temperatures under 9 T. (c) The variation $\Delta\rho_{xy}^{\text{chiral}}$ with the magnetic field. (d) The decrease of $\Delta\rho_{xy}^{\text{chiral}}$ with increasing temperature, and an inset showing the Hall resistivity variation with the magnetic field at a temperature of 6 K.

[33], PdTe_2 [16], PtTe_2 [15], and MoTe_2 [34] as well as superconducting topological materials [35–38]. However, recent research suggests that PHE can also be observed in topological materials that lack the chiral anomaly [39]. Therefore, PHE is considered a useful tool for studying topological behavior through magneto-transport studies.

The schematic diagram of PHE is represented in the inset of Fig. 2 (c). The standard four-probe technique measures the planar Hall resistivity (ρ_{xy}). The magnetic field is applied along the ab plane or perpendicular to the c axis and rotated around the c axis at an angle ϕ relative to the current I . Experimental Hall resistivity data include normal and planar Hall contributions, with

chiral anomaly-induced Hall resistivity symmetric under an antisymmetric applied field, and the normal Hall resistivity being antisymmetric under an opposite applied field [38, 40–42]. To extract the chiral anomaly contribution, the planar Hall resistivity data is averaged opposite to the magnetic field as follows:

$$\rho_{xy}^{PHE} = \left[\frac{\rho_{xy}(B) + \rho_{xy}(-B)}{2} \right] \quad (1)$$

where $\rho_{xy}(B)$ and $\rho_{xy}(-B)$ are Hall resistivity under applied positive and negative magnetic field directions, respectively. The angular dependence of ρ_{xy}^{PHE} is shown in Fig. 2 (a) and (b), with a period of π and maximum values at $\pi/4$ and $3\pi/4$, consistent with the Planar Hall effect (PHE). In Fig. 2 (a), the variation of planar Hall resistivity is shown at 5 K under different magnetic fields. The variation of $\Delta\rho_{xy}^{chiral}$ with magnetic field strength is proportional to H^2 , as shown in Fig. 2 (c), indicating the possible presence of a topological phase in the 1T-NbSeTe system, similar to NbTe₂ [22]. To extract the chiral anomaly contribution, the ρ_{xy}^{PHE} data is fitted using Eq. (2).

$$\rho_{xy} = -\Delta\rho_{xy}^{chiral} \sin\phi \cos\phi \quad (2)$$

where $\Delta\rho_{xy}^{chiral} = \rho_{\perp} - \rho_{\parallel}$ gives the anisotropy in resistivity due to chiral anomaly. ρ_{\perp} and ρ_{\parallel} represent the resistivity for the magnetic field applied perpendicular and parallel to the current direction, respectively. In Fig. 2 (b), the variation of planar Hall resistivity data under 9 T magnetic field at different temperatures is shown. The temperature variation of $\Delta\rho_{xy}^{chiral}$ continuously decreases with increasing temperature, as represented in Fig. 2 (d).

Furthermore, the inset of Fig. 2 (d) displays Hall resistivity data (ρ_{xy} vs H) fitted with $\rho_{xy} = R_H H$ (where R_H is the Hall coefficient) for 6 K. The obtained carrier concentration is $2.22(3) \times 10^{21} \text{ cm}^{-3}$.

c. Superconducting properties

Resistivity and magnetization measurements were performed on cleaved crystals (2 mm \times 2 mm). The electrical resistivity vs temperature measurement $\rho(T)$ was conducted over the temperature range of 300 to 1.9 K in the absence of an applied magnetic field, as depicted in Fig. 3 (a). The resistivity shows metallic behavior in the normal state and exhibits a sudden drop at T_c^{onset} of 3.16(1) K due to the superconducting transition, as shown in Fig. 3 (a). The residual resistivity ratio (RRR) is 1.23. In the normal state, the behavior of electrons is influenced by phonons, leading to temperature-dependent behavior. The Bloch-Grüneisen (BG) model [43] can explain the

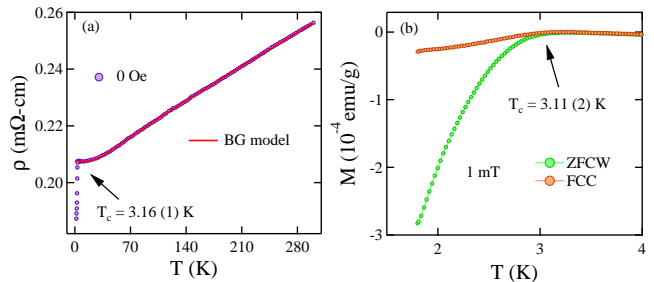


FIG. 3. (a) Temperature variation of resistivity at zero magnetic field, indicating superconductivity with a transition temperature of 3.16(1) K. (b) Magnetization data collected in ZFCW-FCC mode, showing the superconducting transition temperature of 3.11(2) K at an applied magnetic field of 1 mT.

temperature dependence of $\rho(T)$ well. According to this model, the resistivity is given by

$$\rho(T) = \rho_0 + \rho_{BG}(T) \quad (3)$$

where $\rho_{BG}(T)$ is defined as

$$\rho_{BG}(T) = r \left(\frac{T}{\Theta_D} \right)^5 \int_0^{\frac{\Theta_D}{T}} \frac{x^5}{(e^x - 1)(1 - e^{-x})} dx \quad (4)$$

here, ρ_0 represents the residual resistivity, r is a material-dependent constant, and Θ_D is the Debye constant. The fitting parameters obtained using Eq. (4) were $\rho_0 = 0.20(7)$ m Ω cm, $r = 0.11(2)$ m Ω cm, and $\Theta_D = 169(4)$ K, as shown in Fig. 3 (a). The Debye temperature value is found to be similar to the reported value in specific heat for NbSeTe [29].

The absence of a charge density wave (CDW) signal in the normal state resistivity of 1T-NbSeTe distinguishes it from its parent compounds, 1T'-NbTe₂ and 1T-NbSe₂, which exhibit strong CDW even in the monolayer limit [21, 44]. The substitution of selenium in the parent compound may have suppressed the CDW and promoted superconductivity, as reported transition temperatures of 1.3 K [29] and 3.0 K [27, 28] have been observed in 1T-NbSeTe without CDW [27–29]. In our crystal, the recorded superconducting transition temperature is T_c of 3.16 K, which is comparable to the value reported in Ref. [28], revealing that T_c is dependent on the composition.

The temperature dependence of the magnetic moment measurement of 1T-NbSeTe with a superconducting transition at 3.11(2) K is presented in Fig. 3 (b). A 1 mT magnetic field was applied in zero-field cooling (ZFCW) and field-cooled cooling (FCC) modes. The lower critical field $H_{c1}(0)$ is calculated from low-field magnetization measurements for the perpendicular and parallel directions. The M - H curves at various temperatures for

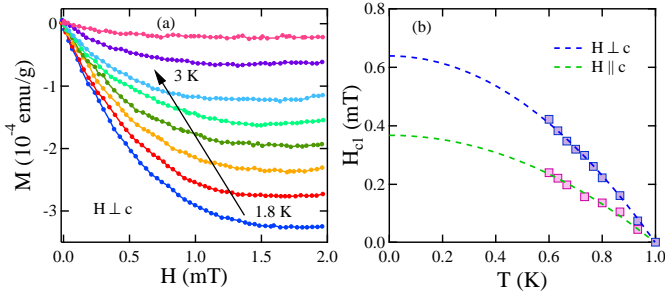


FIG. 4. (a) Low field variation of magnetization data in the perpendicular direction. (b) The lower critical field variation with temperature is well-fitted with GL equations, providing values of 0.63(2) and 0.37(4) mT for the $H \perp c$ and $H \parallel c$ directions, respectively.

$H \perp c$ are illustrated in Fig. 4 (a). The value of $H_{c1}(T)$ is obtained from the point where the Meissner lines deviate for a specific temperature. The Ginzburg-Landau equation Eq. (5) is utilized to fit the values of $H_{c1}(T)$ for both perpendicular and parallel directions of the magnetic field.

$$H_{c1}(T) = H_{c1}(0) \left(1 - \left(\frac{T}{T_c} \right)^2 \right) \quad (5)$$

In Fig. 4 (b), the anisotropy of $H_{c1}(T)$ in two directions is presented. The blue and green dotted lines correspond to the values of $H_{c1}(0)$, which are 0.63 (2) mT and 0.37(4) mT for the $H \perp c$ and $H \parallel c$ directions, respectively.

The upper critical field, $H_{c2}(0)$, was calculated by measuring the isofield resistivity (ρ vs T) in the field range of 0 to 5 T, in both the in-plane and out-of-plane directions of the crystal. $H_{c2}(T)$ values are determined from the 96% drop of the normal state resistivity attributed to disorder. Fig. 5 (a) displays ρ vs T for the perpendicular and parallel (inset) directions of the magnetic field. The $H_{c2}(T)$ data is fitted using the Ginzburg-Landau equation:

$$H_{c2}(T) = H_{c2}(0) \left[\frac{1 - \left(\frac{T}{T_c} \right)^2}{1 + \left(\frac{T}{T_c} \right)^2} \right]. \quad (6)$$

The resulting fits in both directions yield the values of 7.76 (1) T and 2.29 (2) T for the $H \perp c$ and $H \parallel c$ direction, respectively, as shown in Fig. 5 (b). The 2D Ginzburg-Landau model is used to explain $H_{c2}(T)$, with $(1 - T/T_c)^{1/2}$ for $H \perp c$ and $(1 - T/T_c)$ for $H \parallel c$. However, the H_{c2} data points deviated for $H \perp c$, whereas for $H \parallel c$ direction, it is consistent with the 3D model, indicating that quasi-2D superconductivity may be present in the system [45].

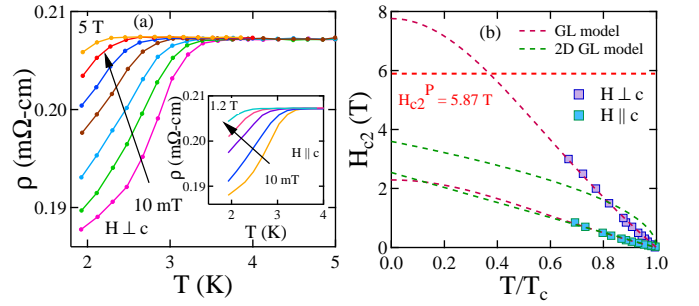


FIG. 5. (a) show the temperature variation of resistivity for different magnetic fields for $H \perp c$ and $H \parallel c$ in the inset. (b) The temperature variation of the upper critical field for two different magnetic field directions fitted with the Ginzburg-Landau equations. The red dotted line indicates the Pauli limit, H_{c2}^P , which is 5.87 T.

In type-II superconductors, Cooper pairs can be broken by the orbital effect and the Pauli paramagnetic effect. In the case of the orbital limiting effect, the increasing kinetic energy of the system destroys Cooper pairs. The orbital limiting field ($H_{c2}^{orbital}$) can be expressed using the Wartherm-Helfand-Hohenberg (WHH) equation [46]:

$$H_{c2}^{orbital} = -\alpha T_c \left. \frac{dH_{c2}(T)}{dT} \right|_{T=T_c}, \quad (7)$$

where α is taken as 0.693 for dirty limit superconductors. For 1T-NbSeTe, the initial slope $-\frac{dH_{c2}(T)}{dT}$ near T_c is calculated to be 2.12(1) T/K using the temperature variation of in-plane upper critical field data, giving an orbital limiting field of 4.64(4) T. However, in the Pauli paramagnetic limit, it is energetically favorable for electron spins to align with the magnetic field, breaking the Cooper pairs. The Pauli paramagnetic limit is expressed as $H_{c2}^P = 1.86T_c = 5.87(7)$ T (shown as the red dotted line in Fig. 5 (b)). Therefore, the upper critical field is 1.32 times higher than the Pauli limiting field. The upper critical fields of comparative materials are listed in Table I. In layered superconductors, violations of the Pauli limit can occur due to strong SOC or finite-momentum pairing. Strong SOC leads to Ising-type superconductivity, which has recently been observed in monolayer 2H-NbSe₂ [50]. Finite-momentum pairing can lead to the Fulde-Ferrell-Larkin-Ovchinnikov (FFLO) state [49]. More low-temperature angle-dependent measurements and theoretical inputs are required to confirm the exact mechanism of Pauli limit violation.

In addition, a detailed study of the anisotropy in the upper critical field for $H \perp c$ and $H \parallel c$ was conducted by measuring the field-dependent resistivity at 2 K for different angles. The variation of field-dependent resistivity with the angle for 1T-NbSeTe is shown in Fig. 6 (a), where θ represents the angle between the magnetic

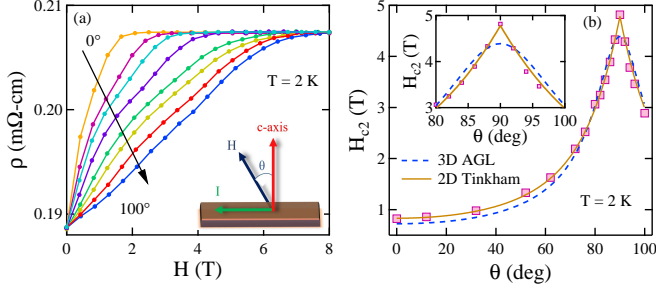


FIG. 6. (a) The field variation of resistivity at a temperature of 2 K. (b) The angle-dependent upper critical field, fitted with both the 3D Ginzburg-Landau model and the 2D Tinkham model.

field and the normal to the sample plane (as depicted in the inset of Fig. 6 (a)). The $H_{c2}(\theta, T)$ values are obtained from the 98% resistivity drop from the normal state value [45, 51]. The anisotropic behavior of the cusp-like upper critical field variation is described using both the 3D anisotropic Ginzburg-Landau model (AGL) and the 2D Tinkham model.

$$\left(\frac{H_{c2}(\theta, T) \sin \theta}{H_{c2}^{\perp}}\right)^2 + \left(\frac{H_{c2}(\theta, T) \cos \theta}{H_{c2}^{\parallel}}\right)^2 = 1 \quad (8)$$

$$\left(\frac{H_{c2}(\theta, T) \sin \theta}{H_{c2}^{\perp}}\right)^2 + \left|\frac{H_{c2}(\theta, T) \cos \theta}{H_{c2}^{\parallel}}\right| = 1 \quad (9)$$

In Fig. 6 (b), the field-dependent resistivity is fitted using the 3D anisotropic Ginzburg-Landau model (AGL) and the 2D Tinkham model, represented by the dotted blue and solid green lines, respectively. The zoomed part in the inset of Fig. 6 (b) shows that the 2D Tinkham model provides a better fit, indicating the possible presence of 2D superconductivity in the bulk single crystal 1*T*-NbSeTe [45, 52].

The Ginzburg-Landau coherence length ($\xi_{\perp c}(0) = 119.9(6)$ Å and $\xi_{\parallel c}(0) = 35.4(5)$ Å) are obtained through the equations $H_{c2}^{\parallel}(0) = \frac{\phi_0}{2\pi\xi_{\perp c}^2(0)}$ and $H_{c2}^{\perp}(0) = \frac{\phi_0}{2\pi\xi_{\parallel c}(0)\xi_{\perp c}(0)}$ [53]. Utilizing these coherence lengths and the lower critical field values ($H_{c1}^{\perp}(0) = 0.63(2)$ mT and $H_{c1}^{\parallel}(0) = 0.37(4)$ mT), the Ginzburg-Landau penetration depth is calculated to be $\lambda_{\perp c}(0) = 1482(9)$ nm and $\lambda_{\parallel c}(0) = 937(7)$ nm by applying Eq. (10).

$$H_{c1}^{\parallel}(0) = \frac{\phi_0}{4\pi\lambda_{\perp c}^2(0)} \left[\ln \left(\frac{\lambda_{\perp c}(0)}{\xi_{\perp c}(0)} \right) + 0.12 \right] \quad (10)$$

where ϕ_0 ($= 2.07 \times 10^{-15}$ Tm²) is the quantum magnetic flux. Using the two coherence lengths, the Ginzburg-Landau parameter $\kappa_{\perp c}$ is calculated as $123 >$

TABLE I. The comparative superconducting parameters for 1*T*-NbSeTe with some layered compounds

Parameter	1 <i>T</i> - NbSeTe	2 <i>H</i> - NbSe ₂ [47]	NbS ₂ [48]	Ba ₆ Nb ₁₁ Se ₂₈ [49]
H_{c2}^{\perp} (T)	7.76	17.3		8.84
H_{c2}^{\parallel} (T)	2.29	5.3	1.6	0.57
H_{c2}^P (T)	5.87	13.54	10.4	4.27
$\xi_{\perp c}$ (Å)	119.9	78.8	143	240.4
$\xi_{\parallel c}$ (Å)	35.4	24.1	9.7	15.6
$\gamma = \frac{H_{c2}^{\perp}(0)}{H_{c2}^{\parallel}(0)}$	3.39	3.3	7.94	10.53

$\frac{1}{\sqrt{2}}$ by $\kappa_{\perp c} = \frac{\lambda_{\perp c}(0)}{\xi_{\perp c}(0)}$. This suggests that the sample exhibits type II superconducting behavior.

The electron-phonon coupling constant (λ_{e-ph}) is a dimensionless parameter that provides insight into the strength of interactions within the system. Using McMillan's model [54], λ_{e-ph} can be calculated from Θ_D and T_c using 169 K and 3.16 K respectively in Eq. (11), where μ^* is the Coulomb repulsion constant (0.13 in our case).

$$\lambda_{e-ph} = \frac{1.04 + \mu^* \ln(\Theta_D/1.45T_c)}{(1 - 0.62\mu^*) \ln(\Theta_D/1.45T_c) - 1.04} \quad (11)$$

For our sample, the calculated value of λ_{e-ph} is 0.66, which is higher than the reported value of 0.55 for 1*T*-NbSeTe with T_c of 1.3 K. This enhancement in λ_{e-ph} suggests that the weak disorder can increase the electron-phonon coupling and consequently enhance the superconducting transition temperature. This has been observed in other systems, such as weak disorder in 2*H*-TaSe_{2-x}S_x [26], Ir-doped MoTe₂ [38], and Re-doped NiTe₂ [14].

d. Electronic properties and the Uemura plot

A set of equations are solved to determine the electronic mean free path and to verify the dirty or clean limit of the 1*T*-NbSeTe superconductor [55]. The Sommerfeld coefficient, which is related to the quasiparticle number density per volume with mean free path, is given by Eq. (12)

$$\gamma_n = \left(\frac{\pi}{3}\right)^{2/3} \frac{k_B^2 m^* V_{f.u.} n^{1/3}}{\hbar^2 N_A}, \quad (12)$$

where k_B is the Boltzman constant, m^* is effective mass, $V_{f.u.}$ is number density per volume of the quasiparticle,

and N_A is Avogadro number. The relationship between the mean free path l_e , the residual resistivity ρ_0 , and the Fermi velocity is

$$l_e = \frac{3\pi^2 \hbar^3}{e^2 \rho_0 m^* v_F}. \quad (13)$$

The value of the Sommerfeld coefficient used in this study is $5.7 \text{ mJ/mol K}^{-2}$, obtained from the previous report on specific heat measurement for $1T$ -NbSeTe [29]. Using carrier concentration and residual resistivity, the effective mass, Fermi velocity, and mean free path are calculated to be $6.27 m_e$, $0.74 \times 10^5 \text{ m/s}$ and $36.05 (6) \text{ \AA}$, respectively, with a coherence length of $324(2) \text{ \AA}$ [56]. The $\frac{\xi_0}{l_e}$ ratio is 9, indicating that the $1T$ -NbSeTe sample is in the dirty limit.

According to Uemura et al., superconducting materials can be classified as conventional or unconventional based on their T_c/T_F ratio. Unconventional superconductors such as Chevrel phases, heavy fermions, Fe-based superconductors, and high T_c superconductors have a T_c/T_F ratio within the range of $0.01 \leq T_c/T_F \leq 0.1$ [57, 58]. To determine the classification of $1T$ -NbSeTe, the Fermi temperature T_F was evaluated using the equation:

$$k_B T_F = \frac{\hbar^2}{2} (3\pi^2)^{2/3} \frac{n^{2/3}}{m^*} \quad (14)$$

where n is the carrier density of $2.22 \times 10^{27} \text{ m}^{-3}$ and m^* , the effective mass is $6.27 m_e$ for the sample. The calculated Fermi temperature for NbSeTe is $1151(4) \text{ K}$ (as shown in Fig. 7). The obtained T_c/T_F ratio of 0.0027 is in the unconventional range, similar to other unconventional materials, which may indicate the presence of a topological phase.

IV. CONCLUSION

In summary, we have successfully synthesized single crystals of NbSeTe in the trigonal $1T$ phase with space group 164. The material exhibits exotic chiral anomaly-induced PHE with H^2 behavior and has a superconducting transition temperature of 3.16 K . The in-plane upper critical field exceeds the Pauli limit, and the angle-dependent upper critical field suggests the presence of 2D superconductivity, indicating unconventional superconductivity in bulk NbSeTe. Furthermore, the Uemura plot also supports the presence of unconventional superconductivity in this material. The coexistence of topological semimetallic nature and superconductivity in NbSeTe makes it a potential candidate for topological superconductivity. However, further investigations, including angle-resolved photoemission spectroscopy (ARPES), detailed electronic structure calculations, and low-temperature and thickness-dependent

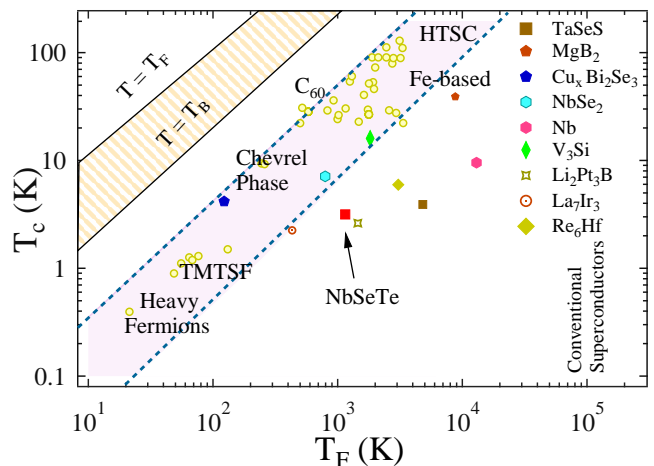


FIG. 7. The plot of the superconducting transition temperature vs the Fermi temperature for different superconducting families. In between, two solid blue lines show the unconventional band of superconductors. NbSeTe lies close to the unconventional band.

measurements, are necessary to fully understand this system's superconducting pairing mechanism.

V. ACKNOWLEDGMENTS

R. P. S. acknowledge Science and Engineering Research Board, Government of India, for the CRG/2019/001028 Core Research Grant.

-
- [1] A. Stern, and N. H. Lindner, Science 339, 1184 (2013).
 - [2] L. Fu, and C. L. Kane, Phys. Rev. Lett. 100, 096407 (2008).
 - [3] R. M. Lutchyn, J. D. Sau, and S. D. Sarma, Phys. Rev. Lett. 105, 077001 (2010).
 - [4] Y. Kasahara, T. Ohnishi, Y. Mizukami, O. Tanaka, S. Ma, K. Sugii, N. Kurita, H. Tanaka, J. Nasu, Y. Motome, T. Shibauchi, and Y. Matsuda, Nature. 559, 231 (2018).
 - [5] M. Sato, and Y. Ando, Rep. Prog. Phys. 80 076501 (2017).
 - [6] S. Friedemann, H. Chang, M. B. Gamza, P. Reiss, X. Chen, P. Alireza, W. A. Coniglio, D. Graf, S. Tozer, and F. M. Grosche, Sci Rep 6, 25335 (2016).
 - [7] H. Wang, and J. Wang, Chinese Phys. B 27 107402 (2018).
 - [8] M. Neupane, S.-Y. Xu, R. Sankar, N. Alidoust, G. Bian, C. Liu, I. Belopolski, T.-R. Chang, H.-T. Jeng, H. Lin, A. Bansil, F. Chou, and M. Z. Hasan, Nat Commun 5, 3786 (2014).
 - [9] Y. Sun, Y. Zhang, C. Felser, and B. Yan, Phys. Rev. Lett. 117, 146403 (2016).
 - [10] H. Wang, H. Wang, Y. Chen, J. Luo, Z. Yuan, J. Liu, Y. Wang, S. Jia, X.-J. Liu, J. Wei, and J. Wang, Sci. Bull. 62, 430 (2017).
 - [11] P. Hosur, X. Dai, Z. Fang, and X.-L. Qi, Phys. Rev. B 90, 045130 (2014).

- [12] P. Tsipas, D. Tsoutsou, S. Fragkos, R. Sant, C. Alvarez, H. Okuno, G. Renaud, R. Alcotte, T. Baron, and A. Dimoulas, *ACS Nano* 2018, 12, 1703 (2018).
- [13] S. Fragkos, P. Tsipas, E. Xenogiannopoulou, Y. Panayiotatos, and A. Dimoulas, *APL Mater.* 9, 101103 (2021).
- [14] M. Mandal, and R. P. Singh, *J. Phys. Condens. Matter* 33 135602 (2021).
- [15] A. Politano, G. Chiarello, B. Ghosh, K. Sadhukhan, C.-N. Kuo, C. S. Lue, V. Pellegrini, and A. Agarwal, *Phys. Rev. Lett.* 121, 086804 (2018).
- [16] H.-J. Noh, J. Jeong, E.-J. Cho, K. Kim, B. I. Min, and B.-G. Park, *Phys. Rev. Lett.* 119, 016401 (2017).
- [17] S. Pyon, K. Kudo, and M. Nohara, *J. Phys. Soc. Jpn.* 81, 053701 (2012).
- [18] H. Chen, Z. Li, X. Fan, L. Guo, and X. Chen, *Solid State Commun.* 275, 20 (2018).
- [19] J. Li, B. Zhao, P. Chen, R. Wu, B. Li, Q. Xia, G. Guo, J. Luo, K. Zang, Z. Zhang, H. Ma, G. Sun, X. Duan, and X. Duan, *Adv. Mater.* 30, 1801043 (2018).
- [20] X. Zhang, T. Luo, X. Hu, J. Guo, G. Lin, Y. Li, Y. Liu, X. Li, J. Ge, and Y. Xing, *Chin. Phys. Lett.* 36, 057402 (2019).
- [21] Y. Nakata, K. Sugawara, R. Shimizu, Y. Okada, P. Han, T. Hitosugi, K. Ueno, T. Sato, and T. Takahashi, *NPG Asia Mater.* 8, e321 (2016).
- [22] S. Gu, K. Fan, Y. Yang, H. Wang, Y. Li, F. Qu, G. Liu, Z. Li, Z. Wang, Y. Yao, J. Li, L. Lu, and F. Yang, *Phys. Rev. B* 104, 115203 (2021).
- [23] K. Zhao, H. Lin, X. Xiao, W. Huang, W. Yao, M. Yan, Y. Xing, Q. Zhang, Z.-X. Li, S. Hoshino, J. Wang, S. Zhou, L. Gu, M. S. Bahramy, H. Yao, N. Nagaosa, Q.-K. Xue, K. T. Law, X. Chen, and S.-H. Ji, *Nat. Phys.* 15, 904 (2019).
- [24] V. D. Neverov, A. E. Lukyanov, A. V. Krasavin, A. Vagov, and M. D. Croitoru, *Commun Phys.* 5, 177 (2022).
- [25] C. Patra, T. Agarwal, R. R. Chaudhari, and R. P. Singh, *Phys. Rev. B* 106, 134515 (2022).
- [26] L. Li, X. Deng, Z. Wang, Y. Liu, M. Abeykoon, E. Dooryhee, A. Tomic, Y. Huang, J. B. Warren, E. S. Bozin, S. J. L. Billinge, Y. Sun, Y. Zhu, G. Kotliar, and C. Petrovic, *npj Quantum Mater.* 2, 11 (2017).
- [27] W. Zhiyuan, H. Yong, Z. Lingyong, L. Zeyu, Q. Zhenhua, L. Huixia, and H. Junfeng, *Acta. Phys. Sin.* 71, 12 (2022).
- [28] C. Li, M. Boubeche, L. Zeng, Y. Ji, Q. Li, D. Guo, Q. Zhu, D. Zhong, H. Luo, and H. Wang, *Phys. Status Solidi RRL* 16, 2100650 (2022).
- [29] D. Yan, S. Wang, Y. Lin, G. Wang, Y. Zeng, M. Boubeche, Y. He, J. Ma, Y. Wang, and D.-X. Yao, *J. Phys. Condens. Matter* 32 025702 (2019).
- [30] H. Luo, W. Xie, J. Tao, H. Inoue, A. Gyenis, J. W. Krizan, A. Yazdani, Y. Zhu, and R. J. Cava, *Proc. Natl. Acad. Sci. USA* 112, E1174 (2015).
- [31] S. Li, Q. Dong, J. Feng, Y. Wang, M. Hou, W. Deng, R. A. Susilo, N. Li, H. Dong, S. Wan, C. Gao, and B. Chen, *Inorg. Chem.* 60, 7864 (2021).
- [32] Y.-Y. Lv, X. Li, B.-B. Zhang, W. Y. Deng, S.-H. Yao, Y. B. Chen, J. Zhou, S.-T. Zhang, M.-H. Lu, L. Zhang, M. Tian, L. Sheng, and Y.-F. Chen, *Phys. Rev. Lett.* 118, 096603 (2017).
- [33] P. Li, C. H. Zhang, J. W. Zhang, Y. Wen, and X. X. Zhang, *Phys. Rev. B* 98, 121108(R) (2018).
- [34] D. D. Liang, Y. J. Wang, W. L. Zhen, J. Yang, S. R. Weng, X. Yan, Y. Y. Han, W. Tong, W. K. Zhu, L. Pi, and C. J. Zhang, *AIP Adv.* 9, 055015 (2019).
- [35] J. Li, Z. Wu, and G. Feng, *J Supercond Nov Magn.* 35, 3521 (2022).
- [36] X. C. Yang, X. Luo, J. J. Gao, Z. Z. Jiang, W. Wang, T. Y. Wang, J. G. Si, C. Y. Xi, W. H. Song, and Y. P. Sun, *Phys. Rev. B* 104, 155106 (2021).
- [37] H. Huang, J. Gu, P. Ji, Q. Wang, X. Hu, Y. Qin, J. Wang, and C. Zhang, *Appl. Phys. Lett.* 113, 222601 (2018).
- [38] M. Mandal, C. Patra, A. Kataria, S. Paul, S. Saha, and R. P. Singh, *Supercond. Sci. Technol.* 35, 025011 (2022).
- [39] A. A. Taskin, H. F. Legg, F. Yang, S. Sasaki, Y. Kanai, K. Matsumoto, A. Rosch, and Y. Ando, *Nat Commun* 8, 1340 (2017).
- [40] T. Li, L. Zhang, and X. Honga, *J. Vac. Sci. Technol. A* 40, 010807 (2022).
- [41] Sonika, M. K. Hooda, S. Sharma, and C. S. Yadav, *Appl. Phys. Lett.* 119, 261904 (2021).
- [42] F. C. Chen, X. Luo, J. Yan, Y. Sun, H. Y. Lv, W. J. Lu, C. Y. Xi, P. Tong, Z. G. Sheng, X. B. Zhu, W. H. Song, and Y. P. Sun, *Phys. Rev. B* 98, 041114(R) (2018).
- [43] M. A. Susner, M. Bhatia, M. D. Sumption, and E. W. Collings, *J. Appl. Phys.* 105, 103916 (2009).
- [44] T. Taguchi, K. Sugawara, H. Oka, T. Kawakami, Y. Saruta, T. Kato, K. Nakayama, S. Souma, T. Takahashi, T. Fukumura, and T. Sato, *Phys. Rev. B* 107, L041105 (2023).
- [45] D. Shen, C. N. Kuo, T. W. Yang, I. N. Chen, C. S. Lue, and L. M. Wang, *Commun. Mater.* 1, 56 (2020).
- [46] B. S. Chandrasekhar, *Appl. Phys. Lett.* 1, 7 (1962).
- [47] F. Soto, H. Berger, L. Cabo, C. Carballeira, J. Mosqueira, D. Pavuna, P. Toimil, and F. Vidal, *Phys. C (Amsterdam, Neth)* 462, 789 (2007).
- [48] K. Onabe, M. Naito, and S. Tanaka, *J. Phys. Soc. Jpn.* 45, 58 (1978).
- [49] K. Ma, S. Jin, F. Meng, Q. Zhang, R. Sun, J. Deng, L. Chen, L. Gu, G. Li, and Z. Zhang, *Phys. Rev. Mater.* 6, 044806 (2022).
- [50] X. Xi, Z. Wang, W. Zhao, J. Park, K. T. Law, H. Berger, L. Forro, J. Shan, and K. F. Mak, *Nat. Phys.* 12, 139 (2016).
- [51] Y. J. Sato, F. Honda, Y. Shimizu, A. Nakamura, Y. Homma, A. Maurya, D. Li, T. Koizumi, and D. Aoki, *Phys. Rev. B* 102, 174503 (2020).
- [52] R. C. Morris, R. V. Coleman, and R. Bhandari, *Phys. Rev. B* 5, 895 (1972).
- [53] M. Konczykowski, C. J. van der Beek, M. A. Tanatar, V. Mosser, Y. J. Song, Y. S. Kwon, and R. Prozorov, *Phys. Rev. B* 84, 180514(R) (2011).
- [54] W. L. McMillan, *Phys. Rev.* 167, 331 (1968).
- [55] Sajilesh K. P., D. Singh, P. K. Biswas, A. D. Hillier, and R. P. Singh, *Phys. Rev. B* 98, 214505 (2018).
- [56] A. Devarakonda, H. Inoue, S. Fang, C. O. Keskinbora, T. Suzuki, M. Kriener, L. Fu, E. Kaxiras, D. C. Bell, and J. G. Checkelsky, *Science* 370, 231 (2020).
- [57] Y. J. Uemura, V. J. Emery, A. R. Moodenbaugh, M. Suenaga, D. C. Johnston, A. J. Jacobson, J. T. Lewandowski, J. H. Brewer, R. F. Kiefl, S. R. Kretzmann, G. M. Luke, T. Riseman, C. E. Stronach, W. J. Kossler, J. R. Kempston, X. H. Yu, D. Opie, and H. E. Schone, *Phys. Rev. B* 38, 909(R) (1988).
- [58] Y. J. Uemura et al., *Phys. Rev. Lett.* 62, 2317 (1989).